Thermal Treatment of Sol-Gel Derived Nickel Oxide Xerogels

CHUAN LIN, SHAHEEN A. AL-MUHTASEB AND JAMES A. RITTER*
*Department of Chemical Engineering, Swearingen Engineering Center, University of South Carolina,
Columbia, SC 29208, USA*
ritter@engr.sc.edu

Abstract.   Very fine nickel hydroxide and oxide xerogel powders were prepared using a new sol-gel synthesis procedure in which nickel ethoxide was produced through the reaction of nickel chloride, as a precursor, with sodium ethoxide in dehydrated ethanol, followed by the hydrolysis of nickel ethoxide with ammonia and drying the resulting hydrogel under subcritical pressures to form the xerogel. The effects of thermal treatment on the surface area, pore volume, crystallinity and particle structure of the resulting xerogels were investigated and found to have significant effects on all of these properties. Overall, the xerogel remained amorphous as $Ni(OH)_2$ up to $200°C$, with little change in the surface area and pore volume. At $250°C$, the $Ni(OH)_2$ began to decompose and form crystalline NiO with the uniformity of the crystals increasing with an increase in temperature. The surface area and pore volume decreased sharply when increasing the temperature beyond $250°C$; this was the temperature where maximums of about 270 m^2/g and 0.33 cm^3/g were exhibited by this composite amorphous $Ni(OH)_2$ and crystalline NiO xerogel powders. At the higher calcination temperatures, very uniform NiO crystals with average crystallite sizes of ~1.7 nm and ~14.5 nm were obtained at 400 and $600°C$, respectively.

Keywords: nickel oxide, nickel hydroxide, sol-gel process, surface area pore volume, nanostructure, thermal effects

1. Introduction

Nickel oxides ($Ni(O_xH_y)_z$) are well-studied materials due to their use in a variety of applications, such as catalysis [1–3], battery electrodes [4–6], and electrochemical capacitors [7, 8]. The preparation methods for these materials basically include impregnation of NiO [9] or $Ni(OH)_2$ [10], solid-state reaction [11], evaporation [12], and electrodeposition [13]. However, these preparation methods usually result in nickel oxides or hydroxides with low surface areas, and this necessarily limits the number of active sites that are available for catalytic and electrochemical reactions. Recently, a novel preparation method, the sol-gel process, is receiving increasing attention in the electrochemical

research community for making metal oxides [14–17]. The sol-gel process is quickly becoming one of the most promising materials synthesis techniques, because it readily allows for control of the texture, composition, homogeneity, and structural properties of the resulting materials [18]. Moreover, numerous studies have recently been devoted to understanding how the synthesis conditions affect the porous structure of sol-gel derived materials [19–23]. Nonetheless, very limited information is available on sol-gel derived ($Ni(O_xH_y)_z$) materials [7, 24, 25], where x, y and z take on values of 1, 1 and 2 for $Ni(OH)_2$ and 1, 0 and 1 for NiO, in this work.

For example, El Baydi et al. [24] reported the production of high surface area (20–55 m^2/g) Ni-containing mixed oxide powders synthesized via a propionic acid sol-gel route for use as oxygen electrocatalysis in

*To whom all correspondence should be addressed.

134   *Lin, Al-Muhtaseb and Ritter*

alkaline media. Serebrenniková et al. [25] investigated the electrochemical behavior of sol-gel produced Ni and Ni-Co oxide films, but no information was provided regarding the corresponding surface areas and pore structures of these films. Liu et al. [7] developed a sol-gel route for making NiO/Ni films for use as an electrochemical capacitor. For the sample fired at 300°C, they reported a Brunauer-Emmett-Teller (BET) surface area of 120 m^2/g.

The objective of this work is to employ a new sol-gel synthesis route [26] for making controlled-pore, high surface area, $Ni(O_xH_y)_z$ structures for use as catalysts, electrode materials, etc. The effects of the calcination temperature on the BET surface area, pore volume, and pore structure of the $Ni(O_xH_y)_z$ xerogels are presented. Transmission electron microscopy (TEM), X-ray diffraction (XRD), thermogravimetric analysis (TGA), and differential scanning calorimetry (DSC) studies were also carried out as a function of the calcination temperature to better elucidate the physical and chemical changes taking place upon heating.

2. Experimental

2.1. Synthesis

Reagent-grade nickel chloride ($NiCl_2$, 98%, Aldrich), sodium ethoxide ($NaOC_2H_5$, 96%, Aldrich), dehydrated ethanol (EtOH, 200 proof, Quantum), and ammonium hydroxide (NH_4OH, 50 vol%, Alfa) were used as received. In a three-necked flask, equipped with a N_2 purge, cooling water condenser, and magnetic stirrer, $NiCl_2$, $NaOC_2H_5$ (mole ratio of $NiCl_2$ to $NaOC_2H_5 = 1:2$), and dehydrated EtOH were added. The mixture was heated and refluxed for 3 h, and then cooled to room temperature. Next, while agitating, a 0.2 M solution of NH_4OH was added dropwise to form the hydrogel; agitation was continued overnight. The reactions are summarized below [17]:

Stage 1: $NiCl_2 + 2NaOC_2H_5$
$\rightarrow Ni(OC_2H_5)_2 + 2NaCl$ (1)

Stage 2: $Ni(OC_2H_5)_2 + 2NH_4OH$
$\rightarrow Ni(OH)_2 + 2NH_4OC_2H_5$ (2)
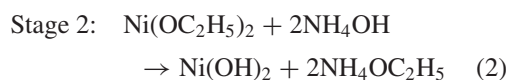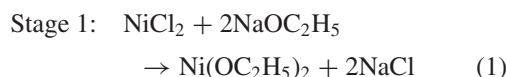
In order to remove the NaCl from the hydrogel, the gel was washed with a 50 vol% solution of EtOH in distilled water and filtered under vacuum three times.

This step was followed by a final wash with 100% dehydrated EtOH.

Temperature-programmed drying and calcination in air were used in the final preparation step. The washed gel was heated to 65°C with a heating rate of 0.5°C/min, and held at 65°C for 5 h. Then, it was heated to 110°C and held there for another 5 h. Finally, it was heated at a rate of 5°C/min to the calcination temperature (varied as a parameter in this study) and held there for 3 h.

2.2. Characterization

A Micromeritics Pulse Chemisorb-2700^{TM} analyzer was used to obtain the BET surface areas and pore volumes of both the carbon xerogels and aerogels. A single point BET method was used to obtain the surface areas using 30 vol% N_2 in He (National Welders). The resulting surface areas were calculated from

$$S = AN\left(1 - \frac{P}{P_0}\right)\frac{V_a}{M}$$ (3)

where V_a is the volume (at STP) of gas adsorbed at a N_2 partial pressure of P (30% of atmospheric pressure), P_0 is the saturation pressure of N_2, A is Avogadro's number (6.023 × 10^{23} molecules/g-mole), M is the molar volume of the gas (22414 cm^3/g-mole at STP) and N is the area of each adsorbed N_2 molecule (estimated as 16.2 Å^2). A single point method was also used to obtain the total pore volumes using 98 vol% N_2 in He (from National Welders) to fill the pores. The resulting pore volumes were calculated from

$$V_p = \left(\frac{M_1}{M}\right)V_a$$ (4)

where M_1 is the molar volume of liquid N_2 (34.670 cm^3/g-mole), and M and V_a are as defined above (at STP).

The skeletal densities were measured with a Quatachrome Ultrapycnometer 1000^{TM}. The transmission electron micrographs were obtained with a Hitachi H-8000^{TM} transmission electron microscope (TEM), and the X-ray diffraction (XRD) patterns were collected using a Rigaku-D-max B diffractometer equipped with a Cu source. A Perkin-Elmer thermogravimetric analyzer (TGA-7) and a Perkin-Elmer differential scanning calorimeter (DSC-7) were used to determine the weight loss and corresponding energetic response of the dried gel upon calcination in air at a heating rate of 5°C/min.

X-ray diffraction peak widths were used to estimate the average size of the crystallites in the $Ni(O_xH_y)_z$ xerogels from the Scherrer equation [27]:

$$d = \frac{K\lambda}{b \cdot \cos\theta} \quad (5)$$

where d is the crystallite size, K is a constant (taken as 0.9), λ is the incident radiation wavelength (1.5406 Å for Cu K_α radiation), b is the peak width at its half height in terms of 2θ and θ is the angle of the diffraction. Note that the peak with the highest intensity was used to determine the crystallite size. The measured pore volume and skeletal density measurements were used to obtain the particle density from

$$d_p = \frac{1}{V_p + \frac{1}{d_s}} \quad (6)$$

where d_p is the particle density and d_s is the skeletal density.

3. Results

The effects of thermal treatment on the surface area and pore volume of the $Ni(O_xH_y)_z$ xerogels are shown in Fig. 1. Initially, the surface area decreases slightly from 215 to 200 m²/g as the temperature increases from 110 to 200°C; but then it jumps surprisingly to ~270 m²/g at 250°C. Beyond 250°C, the surface area decreases sharply to around 50 m²/g at 400°C, and then slowly reaches 20 m²/g at 600°C. In contrast, the pore volume increases almost linearly from 0.26 to 0.32 cm³/g when the temperature increases from 110 to 250°C. Beyond 250°C, it decreases linearly with temperature down to ~0.07 cm³/g at 600°C.

The effects of the calcination temperature on the XRD patterns of the $Ni(O_xH_y)_z$ xerogels are shown in Fig. 2. At low temperatures between 110 and 200°C the XRD patterns are essentially identical with one small peak at $2\theta = $ ~15°, which corresponds to the (001) phase of $Ni(OH)_2$ crystals, and two broad peaks at $2\theta = 34.5$ and 60°, which are associated with amorphous $Ni(OH)_2$. Following calcination at higher temperatures, the XRD patterns show the characteristic peaks of NiO at 37.1, 43.1, and 62.7°, which correspond to the NiO crystalline phases (111), (200) and (220), respectively. These XRD results are identical to those reported in the literature [28, 29]. Traces of these peaks are first detected in the XRD pattern after calcination at 250°C, and then their intensity increases
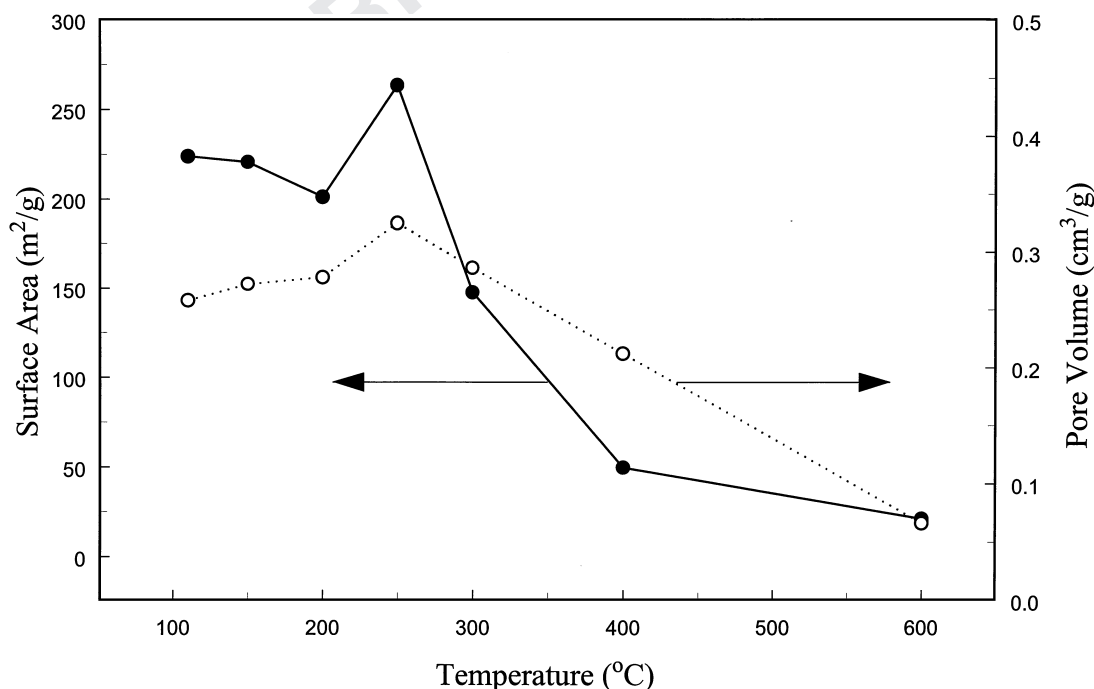
Figure 1.   Effect of the calcination temperature on the surface area and pore volume of $Ni(O_xH_y)_z$ xerogels.

136   *Lin, Al-Muhtaseb and Ritter*
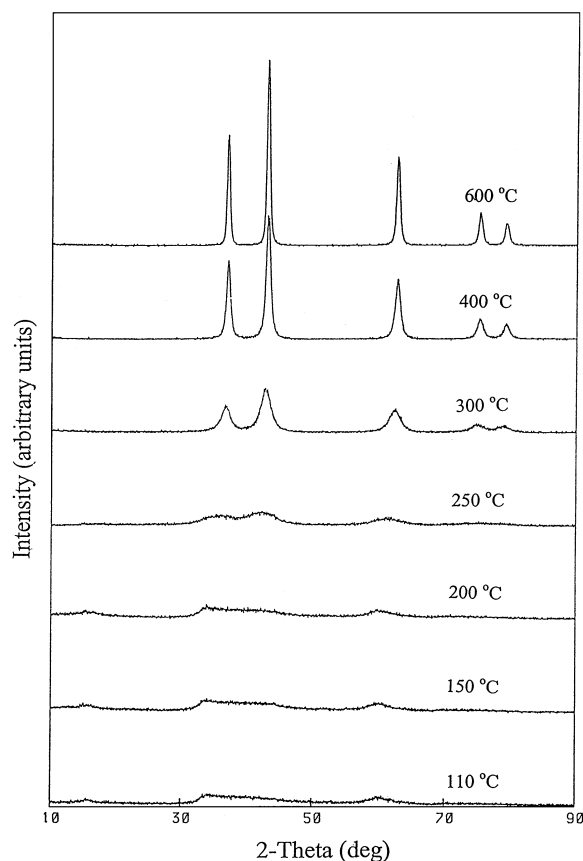
Figure 2. Effect of the calcination temperature on the X-ray diffraction (XRD) pattern of $Ni(O_xH_y)_z$ xerogels.

systematically when increasing the calcination temperature.

The average crystallite size and intensity of the XRD peak at $2\theta = 43.1°$ as a function of the calcination temperature are shown in Fig. 3. Linear, proportionally increasing, dependences on the calcination temperature are exhibited in both cases. The crystallite size is initially $\sim$1.5 nm for the xerogel calcined at 250°C, and it increases to $\sim$14.5 nm as the calcination temperature increases to 600°C. In addition, the increase of the XRD intensity with the calcination temperature indicates that the number of crystallites increases and the xerogel becomes more crystalline.

The TEM images of the $Ni(O_xH_y)_z$ xerogels, dried at 110°C and calcined at 600°C, are shown in Fig. 4(a) and (b), respectively. These images show that the xerogel dried at 110°C is comprised of about 5 nm particles, whereas after calcination at 600°C, the gel particles

increase in size to around 30 nm. The particle sizes of the xerogel obtained from TEM are also two to three times larger than those estimated from XRD. This indicates that the particles seen in the TEM images consist of aggregates of crystallites, instead of single crystallites.

Figure 5 displays the skeletal and particle densities as a function of the calcination temperature. The skeletal density increases almost linearly with temperature from $\sim$2.7 g/cm^3 at 110°C up to $\sim$6.3 g/cm^3 at 400°C, and then remains constant up to 600°C, which is about 95% of the theoretical density [30]. On the other hand, the particle density increases parabolically from $\sim$1.5 g/cm^3 at 110°C to $\sim$4.5 g/cm^3 at 600°C.

The TGA and DSC results are shown in Fig. 6. The weight loss of the xerogels occurs in three stages. An initial weight loss of around 15% is exhibited in the region corresponding to the temperature increasing from ambient temperature ($\sim$25°C) to 200°C. This is followed by a rapid weight loss of around 15% between 200 and 270°C, and then an additional, but gradual, weight loss of around 5% up to 725°C. The initial weight loss up to 200°C is not associated with any appreciable thermal events, as seen in the DSC trace (Fig. 6(b)). However, between 200 and 270°C, the weight loss is accompanied by a marked endothermic event that extends over a broader temperature range (up to $\sim$400°C) than the weight loss. The final small weight loss between 300 and 700°C is accompanied by another marked thermal event; however, in this temperature range an exothermic event occurs.

4. Discussion

The chemistry depicted in Eqs. (1) and (2) gives rise to unique nickel oxides via the hydrolysis and condensation of the transition metal alkoxide. However, because the hydrolysis of the transition metal alkoxide is so rapid [18], this chemistry results in sol-gel derived precipitates instead of monolithic gels. Nevertheless, nickel oxide precipitates can be synthesized with rather interesting properties, as introduced above and discussed below.

The initial decrease in surface area and increase in pore volume when going from 110 to 200°C, as shown in Fig. 1, are essentially attributed to the elimination of some of the internal surface constituents of the $Ni(O_xH_y)_z$ sol-gel (e.g., removal of certain adsorbed
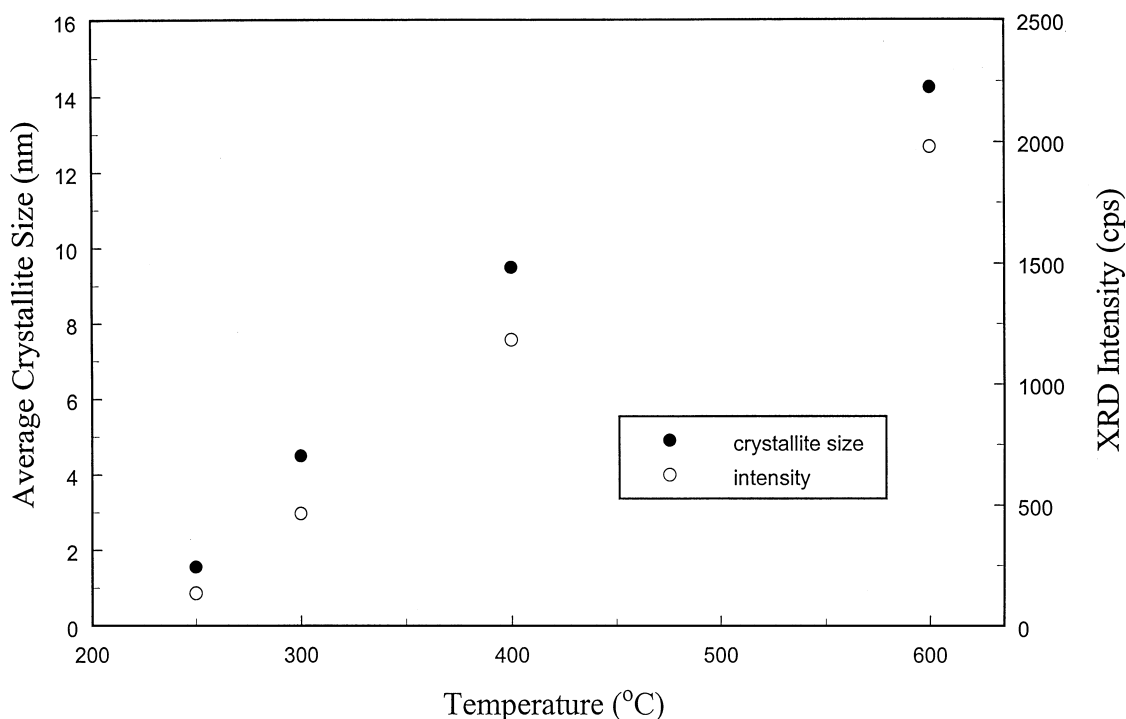
Figure 3. Effect of the calcination temperature on the average crystallite size and the XRD peak intensity of $Ni(O_xH_y)_z$ xerogels at $2\theta = 43.1°$.

species), which leaves extra spaces within the wide pores of the gel structure and also results in a slight reduction of the internal surface area probably due to shrinkage. Due to the synthesis procedure and the temperature range, this behavior is believed to be due to the removal of physisorbed water or some solvent, as well as loosely bound surface hydroxyl groups. The skeletal density increases slightly when increasing the temperature from 100 to 200°C in Fig. 5, which is consistent with the removal of surface hydroxyl groups, which allows the xerogel structure to react further and become more cross-linked. However, at temperatures >200°C, the skeletal density increases sharply with the calcination temperature up to 400°C, indicating substantial removal of tightly bound or even chemisorbed surface hydroxyl groups with subsequent compacting of the skeletal structure in transforming from $Ni(OH)_2$ to NiO as discussed in more detail below. Interestingly, maximum surface areas and pore volumes of the xerogels are exhibited at 250°C in Fig. 1 and most likely due to the initial decomposition of $Ni(OH)_2$ to form NiO through the removal of chemisorbed water according to Eq. (7), which necessarily creates more pores.

$$Ni(OH)_2 \rightarrow NiO + H_2O \qquad (7)$$
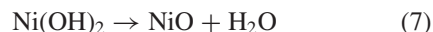
When increasing the temperature from 250 to 600°C, primary NiO crystalline particles start to aggregate and form larger secondary particles, as revealed in Figs. 2 and 3 via the XRD analyses. A sharp drop in the surface area and a gradual drop in the pore volume possibly indicate that the tiny intraparticle voids, i.e., micropores, are virtually eliminated during this step. This is consistent with the XRD results, which show that the XRD intensities and average crystallite size increase significantly when increasing the temperature as shown in Figs. 2 and 3. These secondary particles also continue to grow into even larger crystallites when increasing the temperature from 400 to 600°C, which necessarily eliminates the meso and macropores. Therefore, the pore volume and surface in Fig. 1 both decrease significantly, while the skeletal density in Fig. 5 levels off at 400°C.

The TEM images shown in Fig. 4 indicate that the xerogel particles calcined at low temperatures (i.e.,

138   *Lin, Al-Muhtaseb and Ritter*
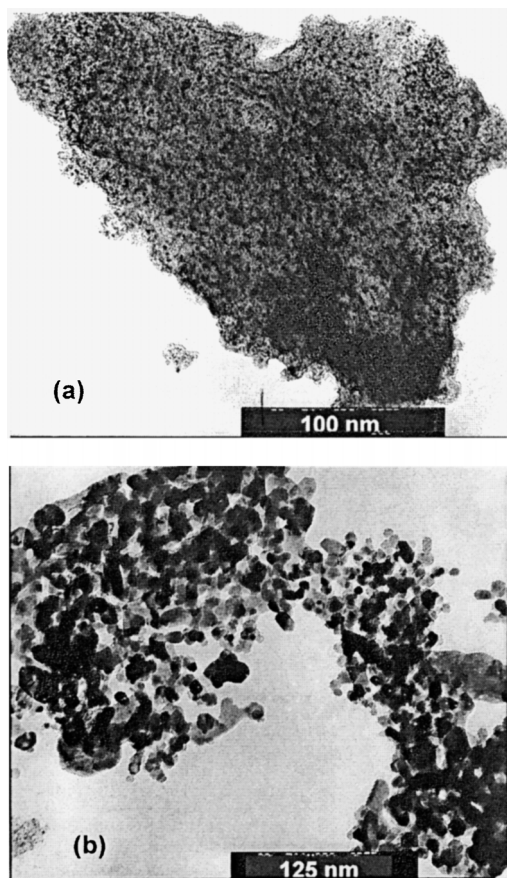
Figure 4. Transmission electron micrograms (TEM) of $Ni(O_xH_y)_z$ xerogels dried at $110°C$ (a) and calcined at $600°C$ (b).

$110°C$, shown in Fig. 4(a)) consist of fine amorphous particles. In contrast, Fig. 4(b) shows that at $600°C$ these fine particles aggregate to form large crystals of NiO. However, it is interesting that the crystalline particle size in Fig. 3 and particle density in Fig. 5 continue to increase as the calcination temperature increases to $600°C$, but that the skeletal density in Fig. 5 levels off at $400°C$. These results indicate that the size of the crystallites increases as a result of cross-linking occurring within the pores as they shrink and loose surface hydroxyl groups; but this occurs without a change in the density of the structural NiO framework. Hence, the pore volume and surface area in Fig. 1 continue to decrease slightly between 400 and $600°C$ until they correspond to only interparticle surface area and void volume at $600°C$.

This interesting result can be illustrated by comparing the surface area determined by the BET method with that calculated from the external particle size observed in the TEM image. Taking, for example, the xerogels calcined at 250 and $600°C$, and supposing that the particle sizes are 20 and 30 nm, respectively (as estimated from the TEM images in Fig. 4), and that the skeletal densities in Fig. 5 are 4.3 and 6.4 g/cm^3, respectively, the external surface areas of (assumed to be) spherical particles can be calculated as 70 and 31 m^2/g, respectively, from the relationship $S = 6/(d_s \cdot \rho)$ where S is the specific surface area, d_s is the skeletal size and ρ is the skeletal density. The calculated surface area of 31 m^2/g is very close to that
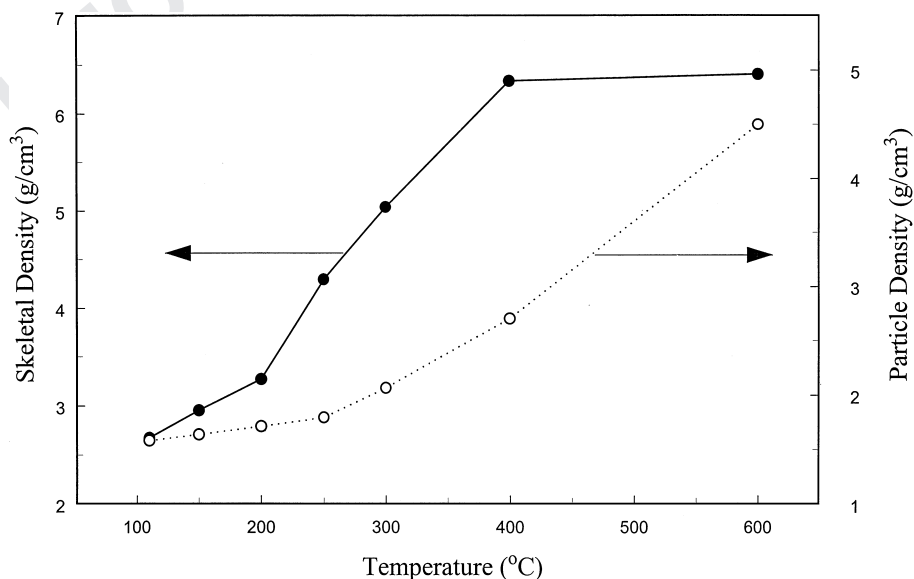
Figure 5. Effect of the calcination temperature on the skeletal and particle densities of $Ni(O_xH_y)_z$ xerogels.
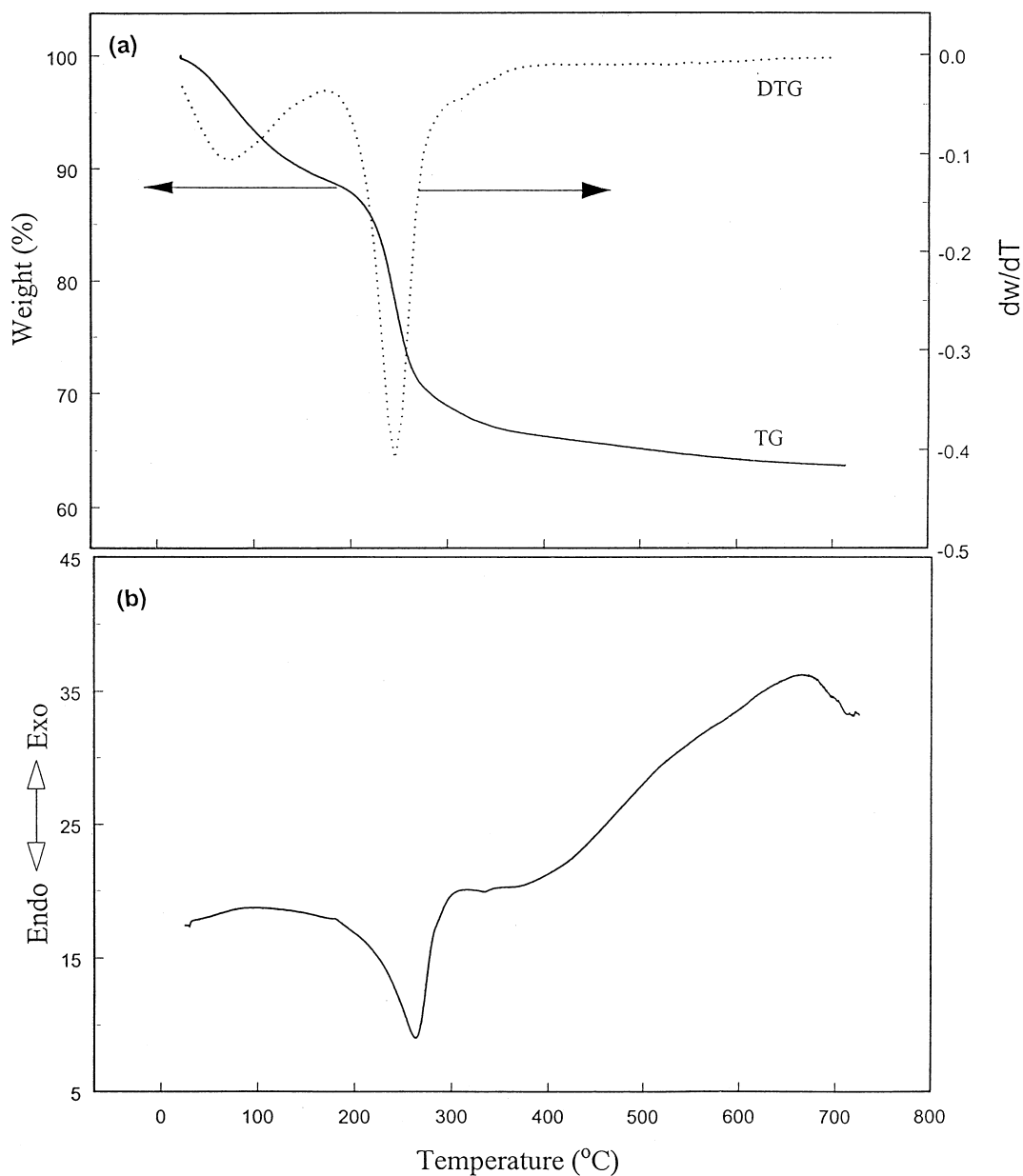
Figure 6.   (a) Thermogravimetric analysis (TGA) and (b) differential scanning calorimetry (DSC) of $Ni(O_xH_y)_z$ xerogels heated in air at 5°C/min.

obtained from the BET measurement for the xerogel calcined at 600°C, which is 25 m^2/g. However, a drastic difference between the calculated (70 m^2/g) and BET (260 m^2/g) surface areas for the xerogel calcined at 250°C is revealed. Hence, at 600°C the NiO xerogel consists of aggregates of nonporous crystals. But between 250 and 400°C significant intra-particle surface area and pore volume can be established within

a structure that is most likely a mixture of crystalline NiO and amorphous $Ni(OH)_2$; and at around 400°C, where it appears that $Ni(OH)_2$ is completely converted to NiO, fairly high surface area (50 m^2/g) NiO particles can be created.

These results are further substantiated by the TGA measurements shown in Fig. 6(a). They reveal a distinct initial region of weight loss between 25°C (ambient

140   *Lin, Al-Muhtaseb and Ritter*

conditions) and 200°C. In accordance with the previous discussions, this region corresponds to the loss of physisorbed water, residual solvent and loosely bound hydroxyl groups, as evidenced also by the marginal changes in the DSC trace shown in Fig. 6(b). This accounted for about 15% of the total weight of the xerogel. The second weight loss region occurs between 200 and 270°C and is accompanied by a significant endothermic heat flow (as shown by the minimum value in Fig. 6(b)), which corresponds to the decomposition of $Ni(OH)_2$ to form NiO; hence, significant structural changes occur within this range of the calcination temperature. The third region, between 270 and 600°C, exhibits only a slight weight loss probably due to the further removal of chemisorbed water through the conversion of $Ni(OH)_2$ to NiO; however, this weight loss is accompanied by a huge exothermic heat flow. This heat flow is believed to be due to structural relaxation [31], where pores are eliminated without significant weight loss. During the structural relaxation of the NiO xerogel, the surface area and pore volume decrease sharply and the particles become larger and more crystalline as shown in Figs. 1 and 2.

5. Conclusions

A sol-gel synthesis route was developed to produce high surface area $Ni(O_xH_y)_z$ xerogel structures, and a number of techniques were used to characterize these materials. Overall, the calcination temperature had a significant impact on the structure of the sol-gel derived xerogel powders. The xerogels exhibited both high surface area and pore volume at relatively low calcination temperatures; but after some characteristic calcination temperature (250°C) was exceeded, both the surface area and pore volume decreased with an increase in temperature. Only very slight changes in the surface area and pore volume were exhibited when the xerogels were calcined at low temperatures (110–200°C), where physisorbed water, residual solvent and loosely bound surface hydroxyl groups were removed from the xerogel. However, maximums in the surface area and pore volume (270 m^2/g and 0.33 cm^3/g) were obtained at 250°C, and then they both decreased sharply when further increasing the calcination temperature up to 600°C. The XRD study revealed that the xerogels calcined with temperatures below 250°C remained amorphous, and that crystallization started at 250°C and then intensified upon further increasing the temperature. At 250°C, the material began to convert from $Ni(OH)_2$

to NiO, which created numerous pores through the removal of chemisorbed water and tightly bound surface hydroxyl groups; beyond 250°C, the pores were eliminated in proportion to the calcination temperature. TGA exhibited a slight weight loss (about 15% of the initial mass) during the removal of the physisorbed species and loosely bound surface hydroxyl groups, with a sharp increase in the weight loss at and beyond 250°C. The reactions accompanying these transitions were highly endothermic at 250°C because of the decomposition of $Ni(OH)_2$ to form NiO; but they eventually became exothermic at higher temperatures because of structural relaxation that occurred without weight loss. The unique properties of these $Ni(O_xH_y)_z$ xerogel powders were attributed to the sol-gel chemistry of transition metal alkoxides.

References

1. G.E.E. Gardes, G.M. Pajonk, and S.J. Teichner, J. Catal. **33**, 145 (1974).
2. K.M. Dooley, S.Y. Chen, and J.R.H. Ross, J. Catal. **145**, 402 (1994).
3. R. Prasad, A. Garg, and S. Mathews, Can. J. Chem. Eng. **72**, 164 (1994).
4. S. Passerini, B. Scrosati, and A. Gorenstein, J. Electrochem. Soc. **137**, 3297 (1990).
5. T. Ohzuku, A. Ueda, and M. Kouguchi, J. Electrochem. Soc. **142**, 4033 (1995).
6. A. Rougier, P. Gravereau, and C. Delmas, J. Electrochem. Soc. **143**, 1168 (1996).
7. K.C. Liu and M.A. Anderson, J. Electrochem. Soc. **143**, 124 (1996).
8. S. Sarangapani, B.V. Tilak, and C.P. Chen, J. Electrochem. Soc. **143**, 3791 (1996).
9. M. Koomiyama, Catal. Rev. **27**, 341 (1985).
10. B. Mani and J.P. de Neufville, J. Electrochem. Soc. **135**, 800 (1998).
11. W.E. O'Grady, K.I. Pandya, K.E. Swider, and D.A. Corrigan, J. Electrochem. Soc. **143**, 1613 (1996).
12. T. Kado and T. Yamada, J. Appl. Phys. **77**, 6651 (1995).
13. S.H. Kim, D.A. Tryk, M.R. Antonio, R. Carr, and D. Scherson, J. Phys. Chem. **98**, 10269 (1994).
14. C. Roger, M.J. Hampden-Smith, D.W. Schaefer, and G.B. Beaucage, J. Sol-Gel Tech. **2**, 76 (1994).
15. Y. Murakami, K. Miwa, M. Ueno, M. Ito, K. Yahikozawa, and Y. Takasu, J. Electrochem. Soc. **141**, L118 (1994).

16. R. Baddour-Hadjean, J. Farcy, J.P. Pereira-Ramos, and N. Baffier, J. Electrochem. Soc. **143**, 2083 (1996).
17. C. Lin, J.A. Ritter, and B.N. Popov, J. Electrochem. Soc. **145**, 4097 (1998).
18. C.J. Brinker and G.W. Scherer, *Sol-Gel Science: The Physics and Chemistry of Sol-Gel Processing* (Academic Press, San Diego, 1990).
19. E.M. Rabinovich, in *Sol-Gel Technology for Thin Films, Fibers, Preforms, Electrons and Specialty Shapes*, edited by L.C. Klien (Noyes, Park Ridg, NJ, 1988).
20. P.J. Davis, C.J. Brinker, D.M. Smith, and R.A. Assink, J. Non-Cryst. Solids **142**, 197 (1992).
21. W.F. Maier, I.C. Tilgner, M. Wiedorn, and H.C. Ko, Advanced Materials **5**, 726 (1993).
22. C. Lin and J.A. Ritter, in *Fundamentals of Adsorption*, edited by M.D. LeVan (Kluwer Academic Publishers, Boston, 1996).
23. C. Lin, J.A. Ritter, and M.D. Amiridis, J. Non-Cryst. Solids **215**, 146 (1997).
24. M. El Baydi, S.K. Tiwari, R.N. Singh, J.L. Rehspringer, P. Chartier, J.F. Koenig, and G. Poillerat, J. Solid State Chem. **116**, 157 (1995).
25. I. Serebrennikova and V.I. Birss, J. Electrochem. Soc. **144**, 566, (1997).
26. Y. Takasu, S. Onoue, K. Kameyama, Y. Murakami, and K. Yahikozawa, Electrochmica Acta **39**, 1993 (1994).
27. H.P. Klug and L.E. Alexander, *X-Ray Diffraction Procedures* (John Wiley and Sons, New York, 1962).
28. K. Nam, W. Yoon, and K. Kim, Electrochimica Acta **47**, 3201 (2002).
29. S. Wang, W. Wang, W. Wang, and Y. Du, Materials Science and Engineering B **90**, 133 (2002).
30. R.C. Weast and M.J. Astle, *CRC Handbook of Chemistry and Physics*, 62nd edn. (CRC Press, Inc., Boca Raton, Florida, 1981/1982).
31. G.W. Scherer, *Relaxation in Glasses and Composites* (Wiley, New York, 1986).